Results in Engineering 24 (2024) 103013

Contents lists available at ScienceDirect

Results in Engineering

journal homepage: www.sciencedirect.com/journal/results-in-engineering

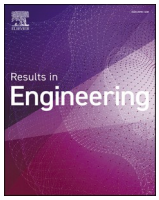

Influence of environmental humidity during filament storage on the structural and mechanical properties of material extrusion 3D-printed poly (lactic acid) parts

László Lendvai [a,*], Imre Fekete [a], Sándor Kálmán Jakab [a], Györgyi Szarka [b], Klára Verebélyi [b], Béla Iván [b]

[a] Department of Materials Science and Engineering, Széchenyi István University, H-9026, Győr, Egyetem tér 1, Hungary
[b] Polymer Chemistry and Physics Research Group, Institute of Materials and Environmental Chemistry, HUN-REN Research Centre for Natural Sciences, H-1117, Budapest, Magyar tudósok krt. 2, Hungary

ARTICLE INFO

Keywords:
Poly(lactic acid)
Material extrusion (MEX)
Fused filament fabrication (FFF)
Environmental conditions
Relative humidity (RH)
Macrostructure

ABSTRACT

Material extrusion (MEX) is one of the most widely used additive manufacturing techniques these days. This study investigates how the properties of MEX 3D-printed objects depend on the relative humidity (RH) conditions in which filaments are stored before and during the manufacturing process. Poly(lactic acid) (PLA) filament was drawn directly from a humidity-controlled chamber into the MEX 3D printer's nozzle. For each set of samples, the filaments were conditioned under different RH conditions, ranging from 10 % to 90 %. The macrostructure of the fabricated products was characterized using computed tomography, revealing increased porosity at higher RH values (from 0.84 % to 4.42 %). The increased porosity at higher storage RH is attributed to under-extrusion and volatile entrapment due to excess moisture. With growing storage RH, the melt flow rate of PLA also gradually increased, indicating a plasticizing effect of humidity on the biopolymer. Gel permeation chromatography and differential scanning calorimetry analyses were conducted to determine whether hydrolytic chain scission took place when PLA was processed in the presence of excessive moisture. Neither measurement indicated any considerable alteration in molecular integrity and crystalline structure as a function of storage RH. Mechanical tests, however, revealed a reduced load-bearing capacity of the manufactured PLA specimens. Flexural strength decreased from 103.0 to 99.6 MPa, and the impact strength dropped from 18.2 to 16.2 kJ/m^2, which is ascribed to the increasing size of pores inside the specimens with increasing storage RH. These findings should be taken into account when designing and processing PLA products by MEX-based additive manufacturing.

1. Introduction

In recent years, additive manufacturing (AM), a cluster of processing methods sharing the common feature of fabricating the desired objects layer by layer [1], has undoubtedly become an essential engineering tool for designing and producing a broad range of products. The various AM machines operating on different principles are commonly denoted as 3D printers [2]. The two major benefits of 3D printing against conventional processing techniques are (i) their ability of manufacturing products without the need for specific machinery or auxiliary tools/molds, and (ii) the fact that they allow the fabrication of complex-shaped objects that would otherwise be challenging or even impossible [3,4]. Additionally, in most cases, the generated material waste is considerably less than in traditional formative and subtractive methods [5]. Due to the above-mentioned advantages, the past three decades have witnessed rapid advances in the field of additive manufacturing, which is already used in a great variety of fields, such as aerospace [6], automotive [7], electronics [8], and biomedical [9] industries and so on.

Among the various AM techniques, the most commonly used ones are the material extrusion (MEX)-based methods, often referenced as Fused Deposition Modeling (FDM), Fused Filament Fabrication (FFF) or Fused Filament Extrusion (FFE) [10–12]. The reason for material extrusion being the most widespread method among 3D printing techniques is that it can produce objects with decent strength and toughness at a relatively

* Corresponding author. H-9026, Egyetem tér 1., Győr, Hungary.
E-mail address: lendvai.laszlo@sze.hu (L. Lendvai).

https://doi.org/10.1016/j.rineng.2024.103013
Received 6 June 2024; Received in revised form 30 August 2024; Accepted 24 September 2024
Available online 26 September 2024

high printing speed, low expense, and with simple machinery [13,14]. These latter features have also made this technique popular among individual "home users" around the world. MEX 3D printers use solid materials in the form of spooled filaments. Even though some printers are capable of working with low melting point metals too, the majority of filaments are made of thermoplastic polymers, such as acrylonitrile-butadiene-styrene (ABS), poly(lactic acid) (PLA), polyethylene terephthalate glycol (PETG), polyamide 6 (PA6), polycaprolactone (PCL), etc. [15,16]. Among the users, there is a great variety of expectations regarding the properties of printed products depending on their intended function, which has facilitated intensive research and development in this field over the last several years [14,17–19].

During the MEX 3D printing process, polymeric filaments are brought into a molten state inside a heated printer head (nozzle). The nozzle then moves horizontally, parallel to the plane of the build platform (X–Y direction), to deposit thin strings, so-called beads, onto the platform. Once the bead cools down, it solidifies and integrates with the neighboring beads. After finishing the current layer of the printed part, the build platform moves away from the nozzle in the Z-direction, and another layer is deposited onto the previous one [3,20]. This process is repeated until the top layer is finished and the product is complete. The printing parameters, such as layer thickness, printing orientation, nozzle temperature, etc., have a fundamental impact on the mechanical and thermal properties, dimensional accuracy, and surface quality of the fabricated product [21]. Consequently, recent trends in MEX-based 3D printing have led to a proliferation of studies focused on understanding of the effects of printing parameters on the properties of fabricated parts [20,22–28].

Currently, the most commonly used polymer for MEX is PLA, owing to its relatively low melting temperature (usually in the range of 150–180 °C), minimal warping, and the broad application possibilities of its 3D-printed objects [29–36]. It has to be noted that PLA is one of the most widely investigated and used biocompatible, biodegradable, and environmentally benign, industrially produced macromolecular materials. PLA is a linear aliphatic thermoplastic copolyester with relatively high strength and stiffness. It is derived from renewable resources, and as a biodegradable material, it is also compostable. With increasing environmental awareness, PLA has gained considerable interest due to these features, finding applications ranging from the food industry to drug release matrices, biodegradable implants, scaffolds for tissue engineering, nanocomposites, and even recyclable products (see, e.g. Refs. [29–51] and references therein). The biodegradability of aliphatic polyesters like PLA, originates from the fact that the ester groups in the chain molecule's backbone are susceptible to chemical hydrolysis in aqueous environments [52,53]. Hydrolytic chain scission of the ester linkage is also the fastest and most effective degradation process that polyesters undergo during processing. As a consequence, the presence of weak hydrolyzable bonds makes PLA extremely sensitive to high temperature and moisture. The scission of ester groups by hydrolysis depends greatly on moisture content, and can occur during melt processing of PLA, resulting in reduced molecular weight along with deteriorating mechanical properties [54]. Several studies have already pointed out that higher moisture content in PLA leads to more intense degradation during processing [55,56]. Therefore, PLA is always dried before melt processing under industrial conditions to prevent degradation. However, most individual users involved in 3D printing tend to neglect this aspect, making the quality of the additively manufactured objects dependent on environmental conditions, which are influenced by a number of factors, even geographical location.

Besides facilitating degradation, the moisture content of the printing material affects the quality of the fabricated objects in other ways as well. For instance, it can have a considerable impact on the melt viscosity of the polymer. According to the literature [57], using filaments with lower moisture content generally results in better structural and mechanical properties of the printed objects. Water, being a low molecular weight liquid, acts as a plasticizer in a broad range of polymeric materials by reducing the viscosity and glass transition temperature of the plastic. Since the equilibrium moisture content of the polymer filament increases with rising relative ambient humidity, environmental conditions can have a direct impact on the printing quality. There is a further issue related to the moisture content, namely the swelling of the material. Halidi and Abdullah [58] investigated the effect of humidity on the properties of ABS filaments and found that the diameter could increase by ~5 % when exposed to a high-moisture environment for an extended period, potentially leading to filament clogging. Since the temperature of the 3D printing process greatly exceeds the boiling point of water, water evaporates during printing. As a consequence, the actual volume of polymer being extruded from the 3D printer nozzle is less than the input volume due to water evaporation, resulting in narrower beads being deposited onto the build platform. Even though environmental temperature and humidity are crucial factors affecting the quality of 3D-printed objects, relatively few studies have examined their effects. Fang et al. [57] investigated how these parameters influence the geometrical and strength properties of 3D-printed parts using polycarbonate filaments. Under the various manufacturing conditions they applied, the authors determined the water content of the material to be in the range of 0–0.15 %. In their study, the authors found a 30 % reduction in mechanical properties in the longitudinal direction relative to the printing orientation and a 70 % reduction in the transverse direction when wet filaments were used. Laumann et al. [59] investigated the influence of filament moisture on adhesion between the printing material and the build platform using PLA, polyvinyl alcohol, and PA6 as feedstock. The authors found that the moisture content of the printing material can alter the adhesion between the printed part and the build surface by up to 68 %, which is a considerable issue as poorer adhesion often leads to intense warping of the printed product.

As outlined above, the moisture absorbed by filaments used for 3D printing is a major factor influencing the quality of the products prepared from them, and it needs to be considered during engineering applications. To the best of the authors' knowledge, no prior investigation has examined the effect of environmental humidity during filament storage on the structural and mechanical properties of MEX 3D-printed PLA products. In this current work, it was explored how systematically varied ambient humidity, in which the filaments are stored before and during printing, affects the macrostructure, molecular weight distribution, thermal properties, and mechanical behavior of 3D-printed objects fabricated by the MEX technique. The macrostructure and porosity of the 3D-printed specimens were examined by computed tomography (CT). Molecular and thermal properties were investigated by gel permeation chromatography (GPC) and differential scanning calorimetry (DSC). The melt flow of the polymers was analyzed by melt flow rate (MFR) measurements, while the mechanical behavior of the samples was examined by flexural and Charpy impact tests. The results of these systematic investigations are expected to lead to the design and processing of PLA products with improved properties for a variety of applications.

2. Materials and methods

2.1. Materials

The polymer filament used in this work was "Extrafill Traffic White" type PLA, purchased from Fillamentum Manufacturing (Hulín, Czech Republic). The official datasheet identifies that no component other than PLA was used for the filament fabrication. The filament had a nominal diameter of 1.75 ± 0.05 mm and a density of 1.24 g/cm^3. Due to precaution, the actual size was determined before the experiments using a micrometer caliper and it was found to be in a smaller range of ±0.02 mm. According to its datasheet, this polymer grade is particularly sensitive to moisture during the 3D printing process, leading to decreased mechanical properties, embrittlement, and stringing as

reported by the manufacturer.

2.2. Processing

Prior to 3D printing, the filament was stored in an Angelantoni ACS DY110 humidification chamber (Massa Martana, Italy) for at least 24 h at 35 °C under various relative humidity (RH) conditions. The lower (10 %) and upper (90 %) limits of RH were chosen based on the limitations of the climate chamber used for the experiments, while the interim range was divided into a reasonable number of steps. Accordingly, five sets of specimens were fabricated in total, with RH values set at 10 %, 30 %, 50 %, 70 %, and 90 % during storage, and the prepared samples were designated as RH_10, RH_30, RH_50, RH_70, and RH_90, respectively. The storage conditions were maintained throughout the entire 3D printing process, with the filaments being directly fed from the humidification chamber through a 2.5 mm diameter hole to the printer's nozzle. To prevent the filament from absorbing or dissipating moisture from/to the environment, it was protected by a silicon tube between the climatic test chamber and the 3D printer. A schematic view of the setup is shown in Fig. 1.

The specimens were fabricated using a commercially available CraftWare Craftbot Plus MEX-type desktop 3D printer (Budapest, Hungary). The samples were printed with an infill orientation parallel to the length of the specimen (raster angle = 0°). The nozzle temperature, nozzle diameter, bed temperature, theoretical infill density, layer thickness, and print velocity were set at 215 °C, 0.4 mm, 60 °C, 100 %, 0.2 mm, and 60 mm/s, respectively. Two shell layers with a thickness of 0.4 mm were applied. During printing, an extrusion multiplier of 1.03 was used, based on preliminary experiments [23], to achieve bulk samples with minimal inherent porosity. The printer head's toolpath was generated using the dedicated CraftWare 1.23 slicer software.

2.3. Characterization

Computed tomography (CT) was used for the porosity analysis of the printed specimens. Segments of 10 mm length (in the Y direction) from the middle of the 3D-printed rectangular specimens were scanned in order to map the locations and extent of the voids. A large envelope industrial tomography system (Yxlon, Hamburg, Germany) was used for scanning the parts, which is capable of scanning small objects as well. The system was equipped with a 225 kV micro-focus X-ray tube and a 409.6 × 409.6 mm detector with a resolution of 1024 × 1024 pixels. The X-ray tube was set to 190 kV acceleration voltage and 1200 μA current. The detector captured 1620 projections with exposure times of 2 s over one revolution of the scanned sample. The projected images served as input for reconstructing the slice images of the specimens. The reconstructed 1024^3 voxel array had a voxel size of 0.015 mm. The reconstructed data was processed using VGStudioMAX 2.2 image processing software (Heidelberg, Germany) along with visual inspection. The samples were aligned in 3D space to compensate for small misalignments. Porosity analysis was conducted to quantify the porosity of the parts and the morphology of the voids. Porosity was calculated as the ratio of the volume of the voids to the total object volume, expressed as percentage.

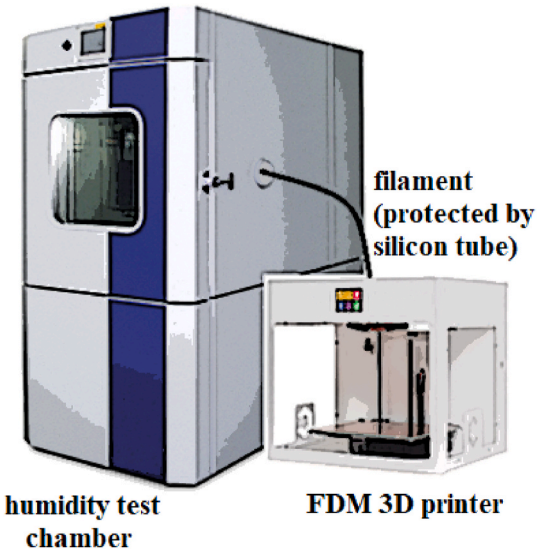

Fig. 1. Schematic view of the 3D printing setup used for fabricating the specimens with the PLA filament directly drawn from the humidity test chamber.

The molecular weight distribution and average molecular weights of the samples were determined by gel permeation chromatography (GPC) analysis with tetrahydrofuran (THF), as the eluent, at a flow rate of 0.3 mL/min. In order to break possible polymer aggregates, the solutions were heated at 60 °C for 15 min, then allowed to cool to room temperature, and filtered twice with a syringe filter of 0.2 μm. The measurements were carried out with a GPC system comprising a Waters HPLC 515 gel pump (Milford, MS, USA), a Jetstream II Plus thermostat, and a Waters Styragel HR1 and HR4 column set (Milford, MA, USA) calibrated with polystyrene standards. The system was operated at 35 °C, with an Agilent Infinity 1260 differential refractive detector (Santa Clara, CA, USA). Data processing was performed using PSS WinGPC software.

Differential scanning calorimetric (DSC) measurements of the prepared specimens were conducted with a Netzsch DSC 200 F3 device (Selb, Germany) under a nitrogen protective atmosphere. A heat-cool-heat thermal program was performed in the temperature range of 30–200 °C, with the first heating run serving to erase the thermal history of the samples. The heating/cooling rate was set to 5 °C/min, and the sample masses were 5–8 mg. The degree of crystallinity (X_c) was calculated using Equation (1):

$$X_c = \frac{\Delta H_m}{\Delta H_m^{\infty}} \tag{1}$$

where ΔH_m (J/g) is the heat of fusion of PLA during melting, measured by the area of the corresponding endothermic peak, and $\Delta H^{\infty}{}_m$ (J/g) is the enthalpy of fusion of 100 % crystalline PLA (93.7 J/g) [60].

Melt flow rate (MFR) measurements were performed with a Ceast 7026.000 Modular Melt Flow apparatus (Pianezza, Italy) according to the ISO 1133 standard. The applied load was 2.16 kg, and the temperature of the barrel was set at 215 °C, matching the temperature used during the 3D printing process.

Flexural mechanical tests were carried out in accordance with ISO 178 at room temperature, with a crosshead speed of 5 mm/min and a span length of 64 mm. Five specimens with a cross-section of 4 × 10 mm^2 and a length of 100 mm were tested for each sample set using an Instron 5582 universal testing machine (Norwood, USA) equipped with a 10 kN force sensor and a 3-point bending setup.

Impact mechanical properties were tested using a Ceast 6545 pendulum instrument (Pianezza, Italy) equipped with a 2 J Charpy hammer at room temperature, following the ISO 179 standard. Unnotched specimens measuring 80 × 4 × 10 mm^3 were used with a bearing distance of 62 mm. Five consecutive measurements were performed for each sample set. The specimens fabricated for the flexural and Charpy tests are shown in Fig. 2, along with a schematic representation of the infill orientations used.

Statistical analysis was performed for all measurements where applicable. The data was analyzed using analysis of variance (ANOVA) and Tukey's HSD test at a significance level of 5 %.

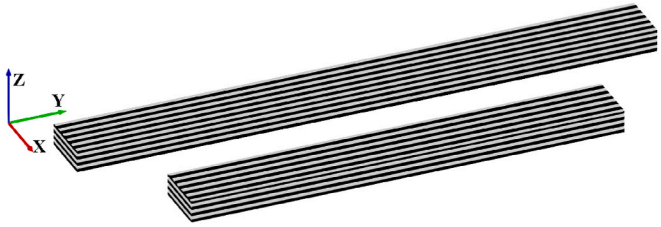

Fig. 2. Schematic 3D model of the printed specimens (hatching represents the orientation, but not the size of the printed beads).

3. Results and discussion

3.1. Micro- and macrostructure

Morphology of the voids can be described using various metrics; in this study, the area of the projected surface of the defect was employed. The three major axes (X, Y, and Z) served as the directions of the projection. Along the Z axis (viewed from above the specimen, or the build direction) the projected area of the void volume was denoted as PZ. Along the Y axis (viewed along the length of the specimens), the projected area was denoted as PY. Finally, the area projection along the X axis was denoted as PX (a perpendicular view to the previous two). A schematic representation of the projection method for a void can be seen in Fig. 3.

The first step was to conduct a visual inspection based on the CT scans shown in Fig. 4, which made the trend of the volumetric size and number of voids in the specimens as a function of storage RH obvious. The void defects inside the specimens that were 3D-printed from filaments stored under higher relative humidity conditions appeared to be larger and more numerous. The voids were mostly located between layers and between beads.

More accurate and quantitative results were obtained through porosity analysis, which revealed the evolution of defects at different RH storage conditions. Fig. 5 shows the defects colored according to the individual defect volumes. Similar to the visual inspection, the analysis reveals a growing size and number of voids with increasing storage RH. When dealing with filaments with high moisture content, one of the most inconvenient issues that can occur is under-extrusion, resulting in a material output lower than optimal. This can be ascribed to two factors: (i) filament slippage between the gears due to its wet filament surface, and (ii) filament swelling that may block the printer's nozzle. A partially clogged nozzle still allows some polymer to flow through but inconsistently, which explains the increased size and volume of voids between the beads. During the analysis of sample RH_90, some voids were detected inside the individual beads as well. This can be attributed to moisture forming entrapped steam pockets when the melt is deposited without rupturing during printing.

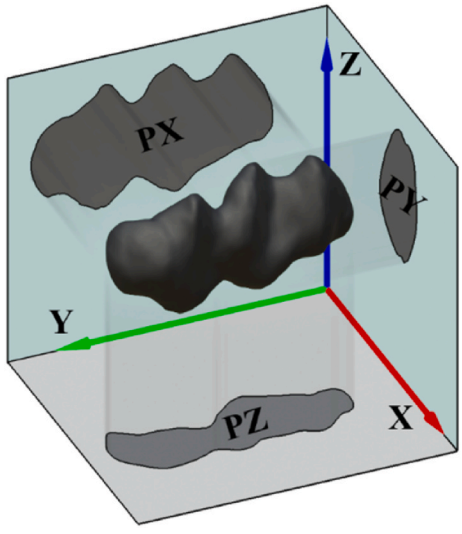

Fig. 3. Schematic view of method for calculating the void projected area along the X, Y, and Z axes.

Further examination of the cross-sections and the detected defects revealed that the porosity distribution along the Z direction is not homogeneous; the bottom layers of the specimens contain considerably fewer voids (if any), and their number gradually increases when proceeding higher along the Z direction. This can be ascribed to the thermal effects of the heated build platform. When printing the first few layers, the temperature of the heated build platform, combined with the extruded hot material and the hot-end of the printer, provides sufficient heat for the previously deposited layer to achieve better fusion with the melt. Meanwhile, at higher layers, the effect of the heated plate is reduced due to the poor thermal conductivity of the polymer and the gradually increasing distance from the heated bed. Due to this thermal mismatch, layers farther from the build platform do not fuse as well as the previous layers, and consequently, they contain more porosity. Similar observations have been previously reported in the literature for MEX-printed products of other thermoplastics [61].

Further information on the porosity analysis, such as the number of voids and the volumetric amount of porosity inside the specimens, was determined through image analysis techniques, the results can be seen in Fig. 6. Based on the data, with increasing storage humidity, a linear increase in porosity can be observed up to ~70 % RH. Above that level, however, the increase in porosity is less pronounced. Regarding the amount of detected voids, their count is relatively constant at lower RH conditions (10–50 % RH). Meanwhile, a steep reduction can be seen from 70 % relative humidity. This is because, during 3D printing at high storage RH conditions, the neighboring beads become almost entirely separated from each other. As a result, a small number of voids are present, but these voids have a very large volume, leading to high porosity values. In contrast, at lower RH levels, the beads were able to locally coalesce with each other, although not along their entire length, resulting in a larger number of small inter-bead voids. This phenomenon is illustrated schematically in Fig. 7.

In Fig. 8, the projected areas of voids are depicted. Individual points in the diagrams correspond to the projected area of a defect along the three main axes. The points are color-mapped according to their PX values (projected area along the X axis, see Fig. 5). The dashed diagonal lines in the diagrams of Fig. 8 represent the theoretical location of the voids, where they would lie if they had a circular shape (equal projected areas along the Z and Y directions). Relative to this line, almost all data points lie above it. Accordingly, almost all voids are suggested to have an elongated shape, rather than spherical. Based on the fact that PY is the lowest among the projected areas, the elongation of voids occurs mainly in the Y direction. This is logical since deposition of beads takes place in this direction during 3D printing. Any discrepancy in the amount of the extruded material results in gaps between the layers and between the beads. Further examination of the diagrams in Fig. 8 helps to understand the formation of the gradually increasing amount of voids with increasing RH from 10 % to 70 %. With increasing relative humidity, the location of the data points shifts in such a way that more and more voids have larger PZ values. This is due to the pores merging in the Y direction, as voids form between two neighboring beads. Further increase in RH (RH $\geq$ 70 %) results in an increase in PX and PY as well. This can be explained by the immense growth of voids, due to their coalescing not only in the Y direction but in the Z direction as well. It also means that the voids between layers get connected. At 90 % relative humidity, fewer individual voids remain because most of them merge into a lower number of large voids that span multiple layers. This behavior explains the drop in the number of voids as presented in Fig. 7. Note that in the case of RH_90, a couple of voids are located along the dashed line (Fig. 8), indicating that they are spherical, as their projected areas are

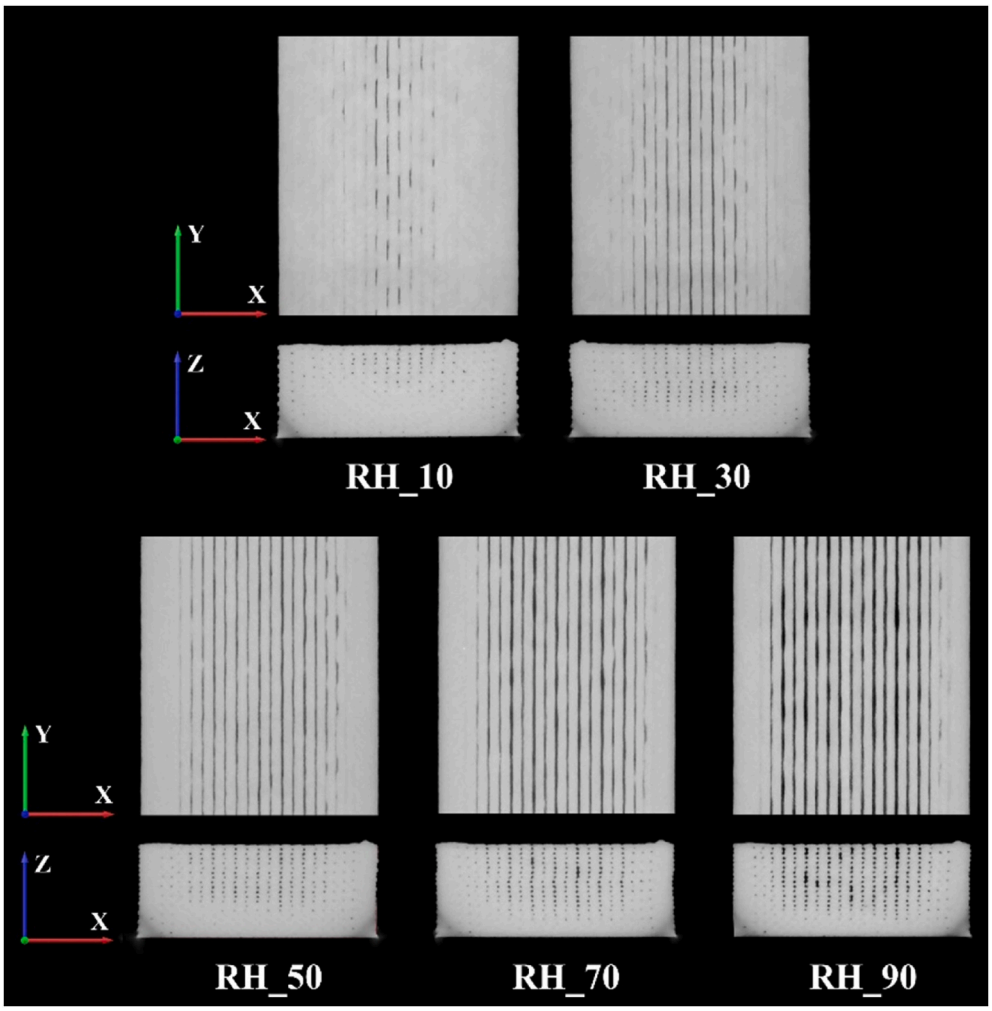

Fig. 4. Cross-sections of specimens 3D-printed at different relative humidity storage conditions.

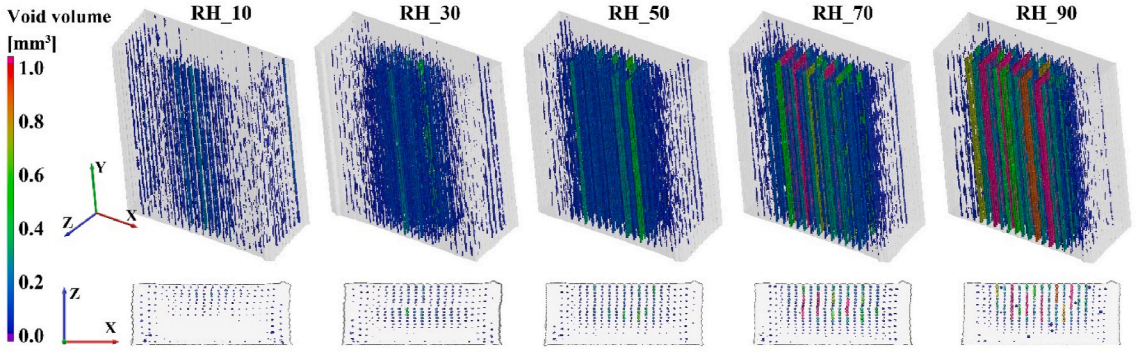

Fig. 5. Porosity analysis results of the specimens printed at different relative humidity storage conditions.

equally sized in all directions (PX ≈ PY ≈ PZ). Considering that at higher RH the inter-bead pores are more likely to elongated, rather than spherical, these outlying data points are suggested to represent the entrapped steam pockets, as previously discussed.

3.2. Molecular weight distribution measurements

In order to determine whether any degradation of PLA occurred due to the presence of moisture during the 3D printing process, the molecular weight distribution (MWD) of the PLA specimens was measured after fabrication. The MWD curves of the 3D-printed specimens at different RH values are shown in Fig. 9. The molecular weight data, specifically the number average molecular weight (M_n), weight average molecular weight (M_w), and peak molecular weight (M_p), are presented in Table 1. The data in Fig. 9 indicate that the MWD curves of the different samples are nearly identical, as they overlap. Therefore, it can be concluded that little to no degradation of PLA occurs during the melt processing of the applied 3D printing technique. This assumption is further supported by the fact that all M_p values fall within a relatively narrow range (142,300–165,800 g/mol). According to the literature,

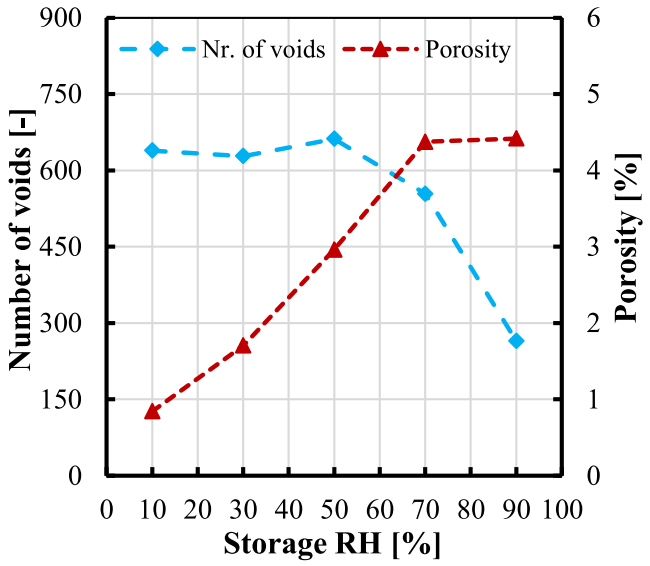

Fig. 6. Detected void count and porosity as a function of relative humidity (RH) storage conditions.

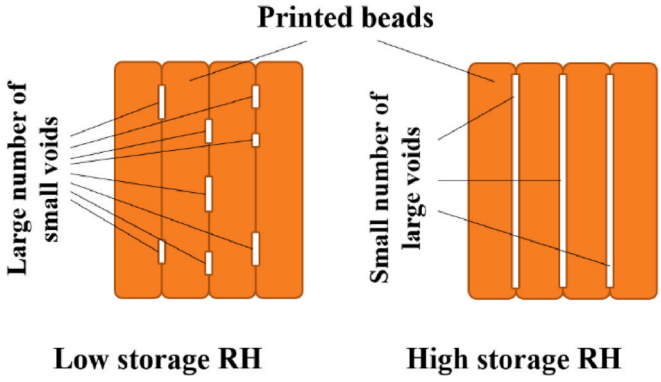

Fig. 7. Schematic illustration of the void number and porosity balance in samples 3D-printed at different storage RH conditions.

extrusion grade PLA types without any degradation also exhibit M_p values within a similar range [62]. Interestingly, although the molecular weight distribution curves are close to each other as shown in Fig. 9, the RH_10 and RH_30 samples possess slightly lower molecular weight

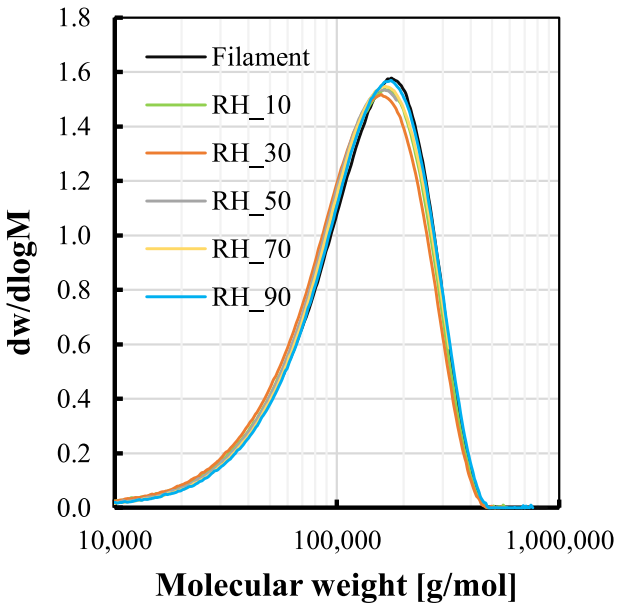

Fig. 9. Molecular weight distribution of PLA samples 3D-printed at different relative humidity values.

Table 1
Molecular weight data derived from the GPC measurements (identical superscript letters within the same column mean no significant difference according to Tukey's honest significance test).

Sample	M_n [g/mol]	M_w [g/mol]	M_p [g/mol]
RH_10	90,100 ± 200^{a}	147,400 ± 700^{a,b}	150,500 ± 3,100^{a,b}
RH_30	88,900 ± 3,200^{a}	143,600 ± 3,500^{a}	142,300 ± 6,000^{a}
RH_50	95,800 ± 1,400^{b}	150,200 ± 1,600^{b,c}	152,200 ± 6,100^{a,b}
RH_70	98,300 ± 900^{b}	151,500 ± 300^{b,c}	160,000 ± 1,100^{a,b}
RH_90	99,700 ± 200^{b}	154,400 ± 500^{c}	156,700 ± 6,500^{b,c}
Filament	95,800 ± 900^{b}	154,400 ± 1,800^{c}	165,800 ± 3,400^{c}

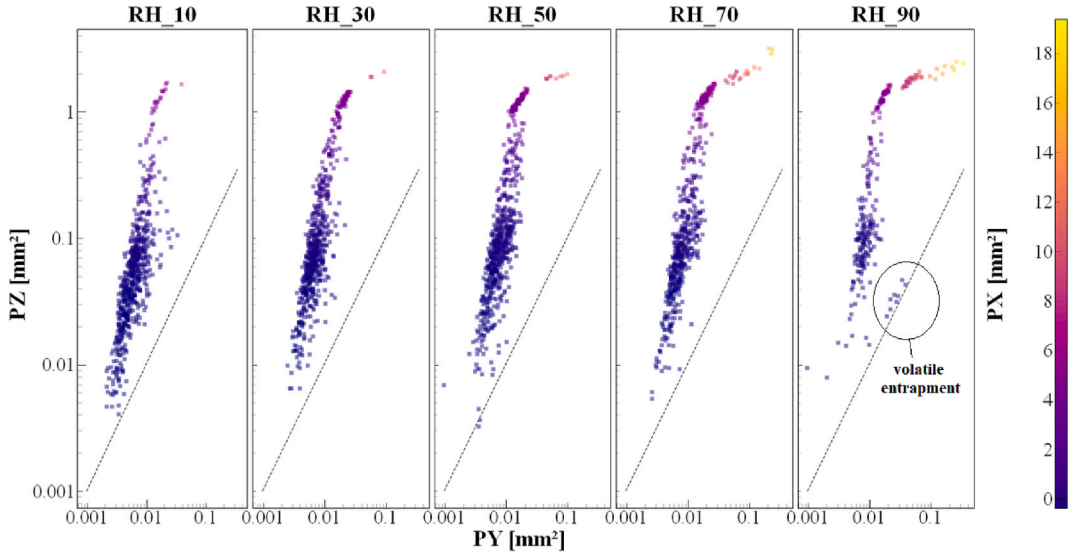

Fig. 8. Scatter plot showing the projected areas of individual voids for each specimen.

values than the filament and samples stored at RH levels at or above 50 %. This can be attributed to some minor chain scission during processing [54,63] due to the lower plasticizing effect by the lower humidity (see MFR data in Section 3.4. Melt flow rate measurements), and as a consequence, to higher shear during processing of the PLA samples stored under lower humidity conditions. Overall, it can be inferred that the relatively brief exposure to high temperatures during the 3D printing process does not induce substantial hydrolytic molecular degradation, related to high humidity levels. In contrast to common polymer processing techniques like extrusion and injection molding, where the polymer melt typically resides in the machine's heated barrel for several minutes, during MEX-type 3D printing, the material stays in its molten state for less than a minute under normal conditions.

3.3. Differential scanning calorimetry

In addition to molecular weight values, changes in characteristic transition temperatures and crystallinity can serve as significant indicators of molecular structure changes, such as degradation, in polymers [64]. This was the primary motivation for conducting DSC analyses on the 3D-printed specimens. The second heating curves recorded during the DSC measurement for each sample are displayed in Fig. 10, and the characteristic temperature values and the extent of crystalline fractions are summarized in Table 2. All samples exhibited four distinct thermal transitions, with the glass transition (T_g) occurring at the lowest temperature. Upon further heating, an exothermic peak corresponding to the cold crystallization (T_{cc}) of the PLA was observed. The presence of this exothermic peak suggests that the material was rather amorphous prior to the heating sequence, which is expected given the relatively slow crystallization kinetics of PLA, preventing it from crystallizing during cooling from the melt. The final two transitions form a double endothermic melting peak, with one peak (T_{m1}) exhibiting a slightly lower temperature than the other (T_{m2}). The double melting of PLA is often attributed to the presence of two crystalline variations, one with a looser packing manner and lower density than the other [65].

Comparing the DSC curves corresponding to the different specimens, it is evident that the T_g values fell within a narrow range of 58.7–59.4 °C, with no apparent trend related to storage humidity. Similarly, the other thermal transition temperatures for the 3D-printed PLA samples were closely aligned, with T_{cc} values between 109.8 and 110.5 °C, T_{m1} values between 148.0 and 148.2 °C, and T_{m2} values between 153.4 and 153.6 °C. The extent of crystallinity across all samples was ~26 %, with no significant differences observed. These findings further support the conclusions drawn from the molecular weight measurements, namely that the relatively brief exposure to high temperatures during 3D printing does not considerably affect the molecular structure of PLA,

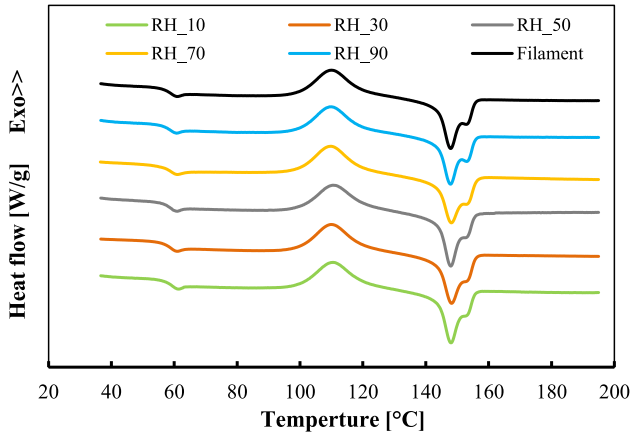

Fig. 10. DSC curves of PLA specimens 3D-printed at different relative storage humidity values.

Table 2
Thermal and crystallinity parameters derived from the DSC results.

Sample	T_g [°C]	T_{cc} [°C]	T_{m1} [°C]	T_{m2} [°C]	ΔH_m [J/g]	X_c [%]
RH_10	58.8	110.5	148.1	153.4	24.0	25.6
RH_30	59.4	110.1	148.3	153.6	24.5	26.1
RH_50	59.3	110.5	148.0	153.5	24.0	25.6
RH_70	58.7	109.8	148.2	153.4	24.8	26.4
RH_90	59.4	110.2	148.2	153.6	23.9	25.5
Filament	59.2	110.3	148.1	153.6	24.0	25.5

even in the presence of relatively high moisture content. Considerable changes in the characteristic molecular weight parameters, i.e. MWD and average molecular weights, and amorphous versus crystalline fractions did not take place as a function of storage conditions. Therefore, the increased porosity observed in the 3D-printed samples cannot be attributed to these factors.

3.4. Melt flow rate measurements

Melt flow rate (MFR) is a useful parameter for determining whether a specific polymer grade is suitable for a given melt processing technique or not. For example, injection molding requires plastics with higher MFR, while extrusion necessitates a lower melt flow rate to produce quality products. Similarly, there is an ideal MFR range for 3D printing filaments; exceeding this range can lead to reduced geometrical accuracy in printed objects due to the low viscosity of the polymer, while falling below it can cause under-extrusion due to increased pressure. The melt flow rate of PLA filament stored under different humidity conditions is shown in Fig. 11. The diagram reveals a gradual increase in MFR as a function of storage RH. The lowest MFR was recorded for the sample RH_10 (10.9 g/10 min) and the highest for RH_90 (19.2 g/10 min). The melt flow rate of a polymer is influenced by various factors, including its molecular weight. Although it might seem reasonable to attribute the increase in MFR to molecular degradation induced by water, the GPC and DSC tests indicated no such deterioration in molecular structure. Another factor that might influence MFR is the presence of secondary components incorporated into the plastic. While stiff, solid particles tend to reduce the melt flow rate, low molecular weight compounds, such as

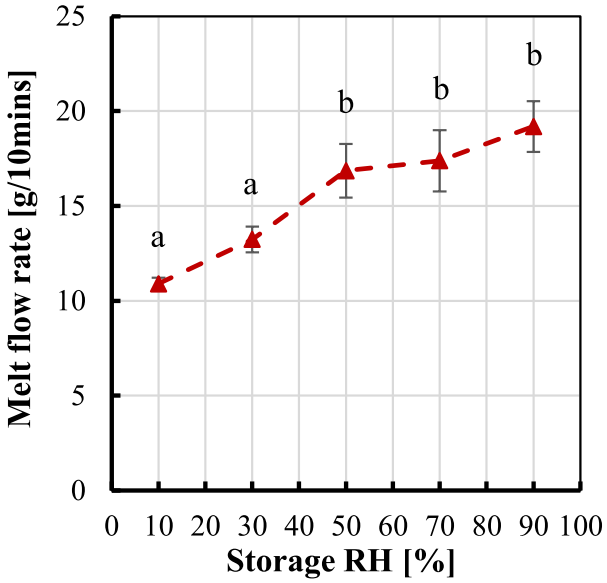

Fig. 11. MFR values of the applied PLA filament determined at 215 °C and 2.16 kg load after conditioning at different RH levels (identical letters above the markers indicate no significant difference according to Tukey's honest significance test).

water diffused among the chain molecules, are likely to increase it. In this context, the absorbed moisture in the filament may act as a plasticizer. This phenomenon is evident in the present case, as the moisture absorbed by the PLA filament under high relative humidity conditions significantly increased the mobility of the polymer chain molecules. This explains the increase in the MFR of PLA, even though its molecular weight remained unchanged. According to the literature, an increase in filament melt flow typically results in lower porosity within the 3D-printed parts due to improved material flow [66]. However, as observed in this study, the presence of water also induced several other side effects, as described in Section 3.1, ultimately leading to an increased porosity.

3.5. Flexural mechanical behavior

Assessing the flexural mechanical properties of 3D-printed objects is essential to prevent potential bending fractures when they are exposed to quasi-static mechanical loads during their application. Therefore, 3-point bending tests were conducted on the MEX 3D-printed parts, and the resulting properties (i.e., flexural strength and modulus), along with typical flexural curves for each sample, are shown in Fig. 12. Fig. 12a illustrates the flexural strength values as a function of storage RH. The results indicate that the load-bearing capacity of the 3D-printed objects decreases as the moisture content of the PLA filament increases. The highest flexural strength (103.1 MPa) was observed for the RH_10 sample, which is comparable to values measured for bulk PLA specimens produced by traditional processing techniques, such as injection molding [67,68]. This is reasonable since this sample contains minimal porosity (<1 %) and can thus be considered as bulk material. When the storage RH was increased to 30 %, 50 %, 70 %, and 90 %, the flexural strength decreased relatively by 2.0 %, 2.2 %, 2.9 %, and 3.4 %, respectively. The relative drop in strength is slightly higher than the percentage increase in porosity of the corresponding specimens (see Fig. 6). Since voids have no load-bearing capacity, it is logical that the strength of the printed objects decreases in proportion to their relative amount. It is important to note that according to the statistical analysis, there was no significant difference in the strength of samples printed between 30 % and 90 % storage RH. Similar trends were observed for the flexural modulus of the 3D-printed specimens (Fig. 12b). The highest modulus (3.51 GPa) was found for the sample printed after conditioning at 10 % RH, with the lowest value (3.41 GPa) observed for the RH_90 sample. The explanation for the reduction in strength due to voids can also be applied to the modulus, as modulus values are proportional to the mechanical stresses arising during the initial stage of the test. Ultimately, based on the results of the flexural tests, it can be concluded that more humid environmental conditions lead to a slight deterioration in quasi-static mechanical properties. This is attributed to the occurrence of voids formed due to under-extrusion rather than to the deterioration of the polymer's molecular structure, which, as discussed based on the results of previously described tests, remained intact.

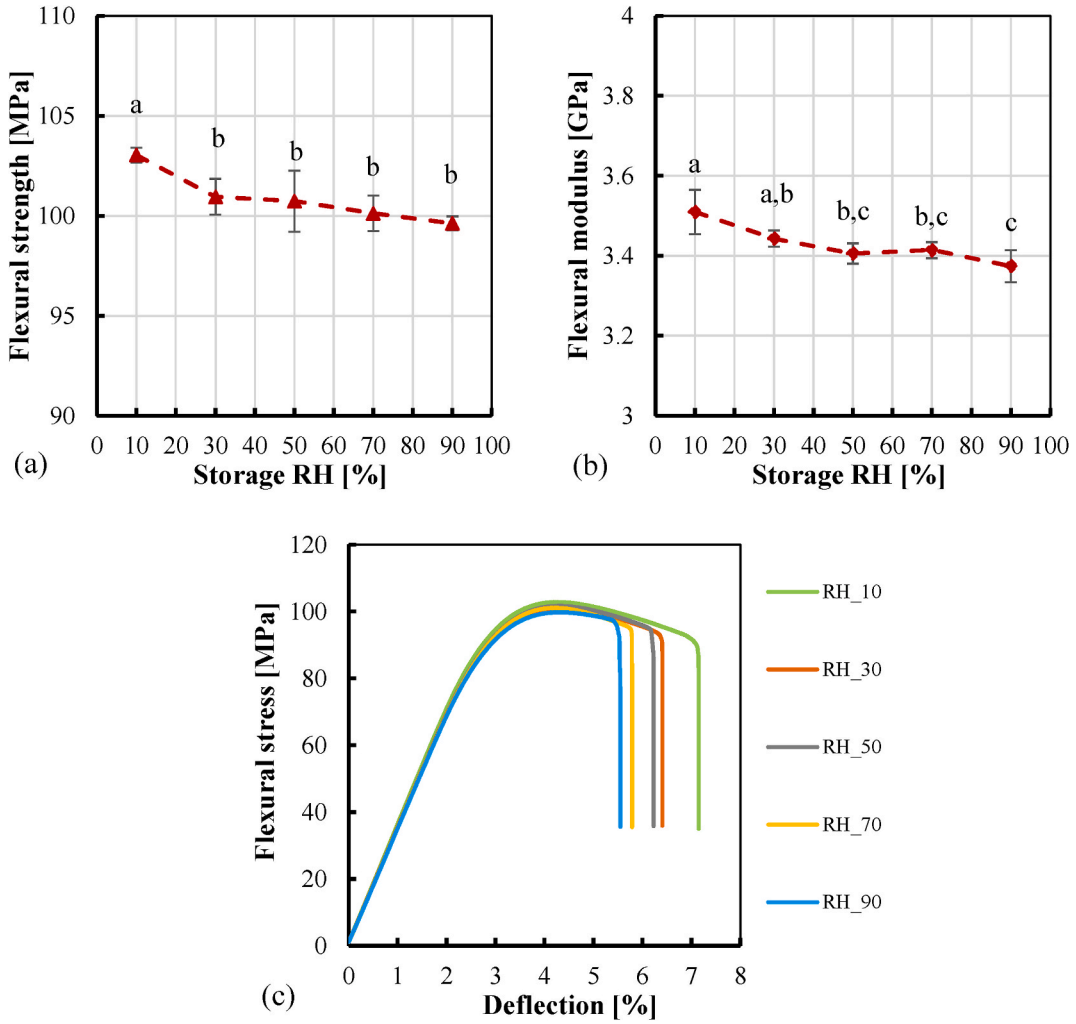

Fig. 12. Flexural strength (a), flexural modulus (b) and typical flexural curves (c) of PLA samples 3D-printed at different RH levels (identical letters above the markers indicate no significant difference according to Tukey's honest significance test).

3.6. Impact strength

The Charpy test was conducted to determine the resistance of the 3D-printed specimens to impact mechanical loads. The measured impact strength values as a function of storage RH are plotted in Fig. 13. Once again, the highest value was observed for the RH_10 sample, with an impact strength of 18.2 kJ/m^2. As storage humidity increased, the relative reductions in impact strength were 4.9 %, 6.8 %, 6.7 %, and 11 % (at 30 %, 50 %, 70 %, and 90 % RH, respectively). These reductions greatly exceed the percentage increase of porosity in the corresponding samples, indicating that the specimens became more sensitive to impact rather than quasi-static fracture. Generally, the mechanical performance of any object decreases as stress concentration occurs at pores or voids. The presence of voids facilitates the development of micro-cracks, especially under impact-like mechanical loads, which subsequently ease crack propagation, explaining this behavior. Once again, the deterioration can be attributed to the development of extensive porosity rather than the degradation of the polymer's molecular structure.

4. Conclusions

Understanding the influence of input parameters during material design, engineering, and manufacturing process is crucial for producing objects with desired properties. When it comes to material extrusion-based 3D printing, the storage conditions of the filament are often neglected. In this study, a comprehensive investigation was conducted to reveal and understand the effect of environmental humidity that was systematically varied in the space where poly(lactic acid) filaments are stored before and during the 3D printing process, on the properties of the printed objects.

Computed tomographic analysis was performed to investigate the micro- and macrostructure of the fabricated specimens, revealing an increasing porosity in the 3D-printed PLAs as a function of the storage relative humidity. At RH conditions ≤70 %, the pores were mainly present in the form of inter-bead voids, with their increasing number indicating under-extrusion attributed to filament swelling-induced clogging. However, at RH levels above 70 %, spherical defects appeared inside the deposited beads, indicating the entrapment of steam pockets as a consequence of rapidly evaporating moisture at the processing temperature. GPC and DSC measurements were applied to determine whether any molecular degradation occurred during the melt processing of filaments stored under various RH conditions. Since no considerable changes in molecular weights were detected, and the characteristic temperatures of the thermal transitions and the extent of crystallinity of PLA were also not altered with increasing RH, it was concluded that moisture does not induce hydrolitic degradation of PLA when exposed to elevated temperatures during 3D printing, even in the presence of excess moisture. Mechanical properties were investigated through flexural and Charpy impact tests. The flexural mechanical properties, including flexural strength and modulus, decreased with increasing RH, in proportion to the increasing porosity. Meanwhile, the drop in impact strength was more pronounced, which is attributed to the fact that during impact-like loads, the material is much more sensitive to the presence of voids, which act as stress concentration sites inside the specimens. These findings on the correlation between relative humidity during storage and the physical properties of the 3D-printed PLA objects are expected to lead to broader consideration in the design, engineering, and manufacturing of products using MEX 3D printing to meet the required criteria for targeted applications.

CRediT authorship contribution statement

László Lendvai: Writing – review & editing, Writing – original draft, Visualization, Validation, Supervision, Resources, Project administration, Methodology, Investigation, Funding acquisition, Formal analysis, Data curation, Conceptualization. **Imre Fekete:** Writing – original draft, Visualization, Software, Methodology, Investigation, Formal analysis. **Sándor Kálmán Jakab:** Investigation, Formal analysis. **Györgyi Szarka:** Investigation, Formal analysis. **Klára Verebélyi:** Investigation, Formal analysis. **Béla Iván:** Writing – review & editing, Writing – original draft, Validation, Methodology, Investigation, Formal analysis.

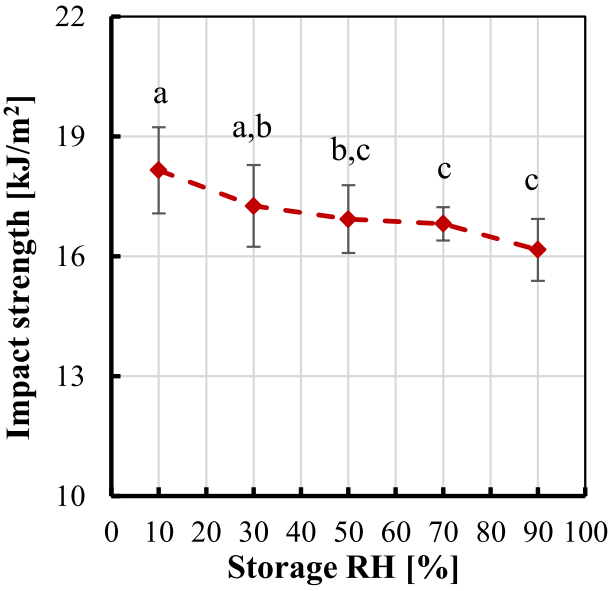

Fig. 13. Charpy impact strength of PLA samples 3D-printed at different RH levels (identical letters above the markers indicate no significant difference according to Tukey's honest significance test).

Declaration of competing interest

The authors declare that they have no known competing financial interests or personal relationships that could have appeared to influence the work reported in this paper.

Data availability

Data will be made available on request.

Acknowledgment

L. Lendvai is grateful for the support of the János Bolyai Research Scholarship of the Hungarian Academy of Sciences. The research presented in this paper was also funded by the "Thematic Excellence Programme 2021 (TKP2021) – National Defence, National Security Subprogramme at the Széchenyi István University (TKP2021-NVA-23).

References

[1] C. Zhai, J. Wang, Y. Tu, G. Chang, X. Ren, C. Ding, Robust optimization of 3D printing process parameters considering process stability and production efficiency, Addit. Manuf. 71 (2023) 103588.
[2] B. Aloyaydi, S. Sivasankaran, A. Mustafa, Investigation of infill-patterns on mechanical response of 3D printed poly-lactic-acid, Polym. Test. 87 (2020) 106557.
[3] M.-H. Hsueh, C.-J. Lai, S.-H. Wang, Y.-S. Zeng, C.-H. Hsieh, C.-Y. Pan, W.-C. Huang, Effect of printing parameters on the thermal and mechanical properties of 3D-printed PLA and PETG, using fused deposition modeling, Polymers 13 (2021) 1758.
[4] A.A. Desai, S. Dnyandev Patil, P.H. Yadav, A. Kekare, Design, analysis, and development of additive manufacturing by using FDM technique with dual nozzle assembly, Mater. Today: Proc. 77 (2023) 619–626.
[5] S.B. Mishra, K. Abhishek, M.P. Satapathy, S.S. Mahapatra, Parametric appraisal of compressive strength of FDM build parts, Mater. Today: Proc. 4 (2017) 9456–9460.
[6] J.C. Najmon, S. Raeisi, A. Tovar, in: F. Froes, R. Boyer (Eds.), Additive Manufacturing for the Aerospace Industry, Elsevier, Amsterdam, Netherlands, 2019. Ch: 2.

[7] X. Gao, N. Yu, J. Li, in: K. Friedrich, R. Walter, C. Soutis, S.G. Advani, I.H.B. Fiedler (Eds.), Structure and Properties of Additive Manufactured Polymer Components, Woodhead Publishing, Duxford, United Kingdom, 2020. Ch: Section 2.3.1.

[8] S.K. Dhinesh, J. Joshua Robert, S. Tushar Nair, D.H. Sharne Moni, S. Sona Fowzeya, K.L. Senthil Kumar, M. Raghunath, P. Nagarajan, Recent trends in additive manufacturing of electronics devices, Mater. Today: Proc. 66 (2022) 928–941.

[9] P. Szymczyk-Ziółkowska, M.B. Łabowska, J. Detyna, I. Michalak, P. Gruber, A review of fabrication polymer scaffolds for biomedical applications using additive manufacturing techniques, Biocybern. Biomed. Eng. 40 (2020) 624–638.

[10] J. Ghorbani, P. Koirala, Y.-L. Shen, M. Tehrani, Eliminating voids and reducing mechanical anisotropy in fused filament fabrication parts by adjusting the filament extrusion rate, J. Manuf. Process. 80 (2022) 651–658.

[11] D. Jungivala, P.K. Gurrala, Finite element analysis of fused filament extrusion build part using different build orientation, Mater. Today: Proc. 38 (2021) 3264–3268.

[12] J. Kattinger, M. Kornely, J. Ehrler, C. Bonten, M. Kreutzbruck, Analysis of melting and flow in the hot-end of a material extrusion 3D printer using X-ray computed tomography, Addit. Manuf. 76 (2023) 103762.

[13] A. Cano-Vicent, M.M. Tambuwala, S.S. Hassan, D. Barh, A.A.A. Aljabali, M. Birkett, A. Arjunan, Á. Serrano-Aroca, Fused deposition modelling: current status, methodology, applications and future prospects, Addit. Manuf. 47 (2021) 102378.

[14] K.B. Mustapha, K.M. Metwalli, A review of fused deposition modelling for 3D printing of smart polymeric materials and composites, Eur. Polym. J. 156 (2021) 110591.

[15] N. Vidakis, M. Petousis, E. Velidakis, M. Liebscher, V. Mechtcherine, L. Tzounis, On the strain rate sensitivity of fused filament fabrication (FFF) processed PLA, ABS, PETG, PA6, and PP thermoplastic polymers, Polymers 12 (2020) 2924.

[16] M. Kováčová, A. Vykydalová, Z. Špitálský, Polycaprolactone with glass beads for 3D printing filaments, Processes 11 (2023) 395.

[17] P.K. Penumakala, J. Santo, A. Thomas, A critical review on the fused deposition modeling of thermoplastic polymer composites, Compos. B Eng. 201 (2020) 108336.

[18] L. Lendvai, I. Fekete, Preparation and characterization of poly(lactic acid)/boehmite alumina composites for additive manufacturing, IOP Conf. Ser. Mater. Sci. Eng. 903 (2020) 012057.

[19] H. Wu, H. Wu, Y. Liu, J. Hu, N. Zhang, X. Wu, Z. Sun, G. Wei, Y. Chen, Y. Duan, J. Zhang, Enhancing the mechanical properties of biodegradable PLLA/PBAT blends for 3D filament via one-pot synthesized CNCs-PVAc powder, Compos. Sci. Technol. 239 (2023) 110064.

[20] M. Daly, M. Tarfaoui, M. Chihi, C. Bouraoui, FDM technology and the effect of printing parameters on the tensile strength of ABS parts, Int. J. Adv. Des. Manuf. Technol. 126 (2023) 5307–5323.

[21] S. Farashi, F. Vafaee, Effect of printing parameters on the tensile strength of FDM 3D samples: a meta-analysis focusing on layer thickness and sample orientation, Progress in Additive Manufacturing 7 (2022) 565–582.

[22] M.T. Birosz, D. Ledenyák, M. Andó, Effect of FDM infill patterns on mechanical properties, Polym. Test. 113 (2022) 107654.

[23] L. Lendvai, I. Fekete, D. Rigotti, A. Pegoretti, Experimental study on the effect of filament-extrusion rate on the structural, mechanical and thermal properties of material extrusion 3D-printed polylactic acid (PLA) products, Progress in Additive Manufacturing (2024), https://doi.org/10.1007/s40964-024-00646-5.

[24] S. Palaniyappan, D. Veeman, S. Narain Kumar, G.J. Surendhar, L. Natrayan, Effect of printing characteristics for the incorporation of hexagonal-shaped lattice structure on the PLA polymeric material, J. Thermoplast. Compos. Mater. 36 (2023) 2009–2030.

[25] S. Palaniyappan, D. Veeman, N.k. Sivakumar, R. Shanmugam, Optimization of compressive property for the development of triply periodic minimal surface lattice structure on polylactic acid polymeric material, J. Reinforc. Plast. Compos. (2022) 07316844221099582. OnlineFirst.

[26] J.A. Naranjo, C. Berges, R. Campana, G. Herranz, Rheological and mechanical assessment for formulating hybrid feedstock to be used in MIM & FFF, Results in Engineering 19 (2023) 101258.

[27] S. Atatreh, M.S. Alyammahi, H. Vasilyan, T. Alkindi, R.A. Susantyoko, Evaluation of the infill design on the tensile properties of metal parts produced by fused filament fabrication, Results in Engineering 17 (2023) 100954.

[28] A. Al Rashid, M. Koç, Experimental validation of numerical model for thermomechanical performance of material extrusion additive manufacturing process: effect of infill design & density, Results in Engineering 17 (2023) 100860.

[29] L. Sandanamsamy, W.S.W. Harun, I. Ishak, F.R.M. Romlay, K. Kadirgama, D. Ramasamy, S.R.A. Idris, F. Tsumori, A comprehensive review on fused deposition modelling of polylactic acid, Progress in Additive Manufacturing 8 (2023) 775–799.

[30] T.M. Joseph, A. Kallingal, A.M. Suresh, D.K. Mahapatra, M.S. Hasanin, J. Haponiuk, S. Thomas, 3D printing of polylactic acid: recent advances and opportunities, Int. J. Adv. Des. Manuf. Technol. 125 (2023) 1015–1035.

[31] N. Fijoł, A. Aguilar-Sánchez, M.-X. Ruiz-Caldas, J. Redlinger-Pohn, A. Mautner, A. P. Mathew, 3D printed polylactic acid (PLA) filters reinforced with polysaccharide nanofibers for metal ions capture and microplastics separation from water, Chem. Eng. J. 457 (2023) 141153.

[32] G. Kharmanda, Challenges and future perspectives for additively manufactured polylactic acid using fused filament fabrication in dentistry, J. Funct. Biomater. 14 (2023) 334.

[33] I. Alonso-Fernández, H.J. Haugen, M. López-Peña, A. González-Cantalapiedra, F. Muñoz, Use of 3D-printed polylactic acid/bioceramic composite scaffolds for bone tissue engineering in preclinical in vivo studies: a systematic review, Acta Biomater. 168 (2023) 1–21.

[34] S. He, S. Hu, Y. Wu, R. Jin, Z. Niu, R. Wang, J. Xue, S. Wu, X. Zhao, L. Zhang, Polyurethanes based on polylactic acid for 3D printing and shape-memory applications, Biomacromolecules 23 (2022) 4192–4202.

[35] S. Sultan, N. Thomas, M. Varghese, Y. Dalvi, S. Joy, S. Hall, A.P. Mathew, The design of 3D-printed polylactic acid–bioglass composite scaffold: a potential implant material for bone tissue engineering, Molecules 27 (2022) 7214.

[36] M.-E. Grigora, Z. Terzopoulou, D. Baciu, T. Steriotis, G. Charalambopoulou, E. Gounari, D.N. Bikiaris, D. Tzetzis, 3D printed poly(lactic acid)-based nanocomposite scaffolds with bioactive coatings for tissue engineering applications, J. Mater. Sci. 58 (2023) 2740–2763.

[37] T.A. Swetha, A. Bora, K. Mohanrasu, P. Balaji, R. Raja, K. Ponnuchamy, G. Muthusamy, A. Arun, A comprehensive review on polylactic acid (PLA) – synthesis, processing and application in food packaging, Int. J. Biol. Macromol. 234 (2023) 123715.

[38] E. Balla, V. Daniilidis, G. Karlioti, T. Kalamas, M. Stefanidou, N.D. Bikiaris, A. Vlachopoulos, I. Koumentakou, D.N. Bikiaris, Poly(lactic acid): a versatile biobased polymer for the future with multifunctional properties—from monomer synthesis, polymerization techniques and molecular weight increase to PLA applications, Polymers 13 (2021) 1822.

[39] H. Ramezani Dana, F. Ebrahimi, Synthesis, properties, and applications of polylactic acid-based polymers, Polym. Eng. Sci. 63 (2023) 22–43.

[40] N.-A.A.B. Taib, M.R. Rahman, D. Huda, K.K. Kuok, S. Hamdan, M.K.B. Bakri, M.R. M.B. Julaihi, A. Khan, A review on poly lactic acid (PLA) as a biodegradable polymer, Polym. Bull. 80 (2023) 1179–1213.

[41] D. da Silva, M. Kaduri, M. Poley, O. Adir, N. Krinsky, J. Shainsky-Roitman, A. Schroeder, Biocompatibility, biodegradation and excretion of polylactic acid (PLA) in medical implants and theranostic systems, Chem. Eng. J. 340 (2018) 9–14.

[42] S. Castañeda-Rodríguez, M. González-Torres, R.M. Ribas-Aparicio, M.L. Del Prado-Audelo, G. Leyva-Gómez, E.S. Gürer, J. Sharifi-Rad, Recent advances in modified poly (lactic acid) as tissue engineering materials, J. Biol. Eng. 17 (2023) 21.

[43] F. Ebrahimi, H. Ramezani Dana, Poly lactic acid (PLA) polymers: from properties to biomedical applications, International Journal of Polymeric Materials and Polymeric Biomaterials 71 (2022) 1117–1130.

[44] A. Ahmad, F. Banat, H. Alsafar, S.W. Hasan, An overview of biodegradable poly (lactic acid) production from fermentative lactic acid for biomedical and bioplastic applications, Biomass Conversion and Biorefinery 14 (2024) 3057–3076.

[45] A. Vlachopoulos, G. Karlioti, E. Balla, V. Daniilidis, T. Kalamas, M. Stefanidou, N. D. Bikiaris, E. Christodoulou, I. Koumentakou, E. Karavas, D.N. Bikiaris, Poly (Lactic acid)-based microparticles for drug delivery applications: an overview of recent advances, Pharmaceutics 14 (2022) 359.

[46] B. Oktay, G.Ö. Eroğlu, S. Demir, S.E. Kuruca, N.K. Apohan, Poly(lactic acid) nanofibers containing phosphorylcholine grafts for transdermal drug delivery systems, Materials Today Sustainability 18 (2022) 100132.

[47] X. Li, Y. Lin, M. Liu, L. Meng, C. Li, A review of research and application of polylactic acid composites, J. Appl. Polym. Sci. 140 (2023) e53477.

[48] R.A. Ilyas, M.Y.M. Zuhri, H.A. Aisyah, M.R.M. Asyraf, S.A. Hassan, E.S. Zainudin, S. M. Sapuan, S. Sharma, S.P. Bangar, R. Jumaidin, Y. Nawab, A.A.M. Faudzi, H. Abral, M. Asrofi, E. Syafri, N.H. Sari, Natural fiber-reinforced polylactic acid, polylactic acid blends and their composites for advanced applications, Polymers 14 (2022) 202.

[49] J. Zhao, G. Wang, J. Chai, E. Chang, S. Wang, A. Zhang, C.B. Park, Polylactic acid/UV-crosslinked in-situ ethylene-propylene-diene terpolymer nanofibril composites with outstanding mechanical and foaming performance, Chem. Eng. J. 447 (2022) 137509.

[50] N.D. Bikiaris, I. Koumentakou, C. Samiotaki, D. Meimaroglou, D. Varytimidou, A. Karatza, Z. Kalantzis, M. Roussou, R.D. Bikiaris, G.Z. Papageorgiou, Recent advances in the investigation of poly(lactic acid) (PLA) nanocomposites: incorporation of various nanofillers and their properties and applications, Polymers 15 (2023) 1196.

[51] J. Chen, Z. Liu, S. Qiu, Y. Li, J. Sun, H. Li, X. Gu, S. Zhang, A new strategy for the preparation of polylactic acid composites with flame retardancy, UV resistance, degradation, and recycling performance, Chem. Eng. J. 472 (2023) 145000.

[52] V. Speranza, A. De Meo, R. Pantani, Thermal and hydrolytic degradation kinetics of PLA in the molten state, Polym. Degrad. Stabil. 100 (2014) 37–41.

[53] P.E. Le Marec, L. Ferry, J.-C. Quantin, J.-C. Bénézet, F. Bonfils, S. Guilbert, A. Bergeret, Influence of melt processing conditions on poly(lactic acid) degradation: molar mass distribution and crystallization, Polym. Degrad. Stabil. 110 (2014) 353–363.

[54] I. Velghe, B. Buffel, V. Vandeginste, W. Thielemans, F. Desplentere, Review on the degradation of poly(lactic acid) during melt processing, Polymers 15 (2023) 2047.

[55] V. Taubner, R. Shishoo, Influence of processing parameters on the degradation of poly(L-lactide) during extrusion, J. Appl. Polym. Sci. 79 (2001) 2128–2135.

[56] Y. Wang, B. Steinhoff, C. Brinkmann, I. Alig, In-line monitoring of the thermal degradation of poly(l-lactic acid) during melt extrusion by UV–vis spectroscopy, Polymer 49 (2008) 1257–1265.

[57] L. Fang, Y. Yan, O. Agarwal, S. Yao, J.E. Seppala, S.H. Kang, Effects of environmental temperature and humidity on the geometry and strength of polycarbonate specimens prepared by fused filament fabrication, Materials 13 (2020) 4414.

[58] S.N.A.M. Halidi, J. Abdullah, Moisture effects on the ABS used for Fused Deposition Modeling rapid prototyping machine, in: 2012 IEEE Symposium on Humanities, Science and Engineering Research, 2012, pp. 839–843.

[59] D. Laumann, D. Spiehl, E. Dörsam, Influence of printing material moisture on part adhesion in fused filament fabrication 3D printing, J. Adhes. 100 (2024) 380–394.

[60] X. Zhang, S. Li, C. Xu, J. Li, Z. Wang, Study on the mechanical and thermal properties of poly(lactic acid)/office waste paper fiber composites, J. Appl. Polym. Sci. 137 (2020) 49390.
[61] M. Rinaldi, T. Ghidini, F. Cecchini, A. Brandao, F. Nanni, Additive layer manufacturing of poly (ether ether ketone) via FDM, Compos. B Eng. 145 (2018) 162–172.
[62] K. Litauszki, Z. Kovács, L. Mészáros, Á. Kmetty, Accelerated photodegradation of poly(lactic acid) with weathering test chamber and laser exposure – a comparative study, Polym. Test. 76 (2019) 411–419.
[63] T. Aldhafeeri, M. Alotaibi, C.F. Barry, Impact of melt processing conditions on the degradation of polylactic acid, Polymers 14 (2022) 2790.
[64] G. Reich, Use of DSC to study the degradation behavior of PLA and PLGA microparticles, Drug Dev. Ind. Pharm. 23 (1997) 1177–1189.
[65] M.L. Di Lorenzo, R. Androsch, Influence of α′-/α-crystal polymorphism on properties of poly(l-lactic acid), Polym. Int. 68 (2019) 320–334.
[66] D. Kuba, R. Matsuzaki, S. Ochi, S. Ogihara, 3D printing of composite materials using ultralow-melt-viscosity polymer and continuous carbon fiber, Composites Part C: Open Access 8 (2022) 100250.
[67] T. Singh, P. Pattnaik, D. Shekhawat, L. Ranakoti, L. Lendvai, Waste marble dust-filled sustainable polymer composite selection using a multi-criteria decision-making technique, Arab. J. Chem. 16 (2023) 104695.
[68] S.K. Jakab, T. Singh, I. Fekete, L. Lendvai, Agricultural by-product filled poly(lactic acid) biocomposites with enhanced biodegradability: the effect of flax seed meal and rapeseed straw, Composites Part C: Open Access 14 (2024) 100464.